JOURNAL OF THERMOPHYSICS AND HEAT TRANSFER
Vol. 6, No. 3, July–Sept. 1992

# Nonequilibrium Chemical and Radiation Coupling, Part II: Results for AOTV Flowfields

Thomas A. Gally* and Leland A. Carlson†
*Texas A&M University, College Station, Texas 77843*

**A flowfield model for the stagnation region of high altitude entry vehicles which includes nonequilibrium chemistry, multitemperature, viscous, conduction, diffusion, coupled nongray nonequilibrium radiative transfer for atoms, and molecules, and local thermodynamic nonequilibrium phenomena has been applied to two Aeroassisted Flight Experiment (AFE) trajectory points, a high-speed return from Mars, a series of points at 80 km for 12–16 km/s, and three altitudes at 16 km/s. Based on these results shock slip is significant, radiation cooling/coupling is minor at AFE conditions but important by 14 km/s and dominant at 16 km/s, radiation for the AFE is small but important and primarily molecular, above 12 km/s atomic radiation is a significant or dominant portion of the total heating, and local thermodynamic nonequilibrium is important and should be included in all cases.**

## Nomenclature

| | | |
|---|---|---|
| $c_p^e$ | = | frozen specific heat at constant pressure, Eq. (4) |
| $c_{p_r}$ | = | specific heat at constant pressure of species $r$ |
| $\mathcal{D}$ | = | binary diffusion coefficient |
| $H$ | = | total enthalpy |
| $HREF$ | = | reference (freestream) total enthalpy |
| $h$ | = | enthalpy |
| $n$ | = | surface normal coordinate axis |
| $p$ | = | pressure |
| $Q_e$ | = | rate of inelastic electron energy exchange |
| $QR+$ | = | radiative flux to wall |
| $q_r$ | = | radiative heat flux |
| $T$ | = | temperature |
| $u$ | = | mass averaged velocity |
| $\dot{w}$ | = | chemical production rate |
| $YSHOCK$ | = | shock standoff distance |
| $y_s$ | = | shock standoff distance |
| $\eta$ | = | heat conduction coefficient |
| $\xi_e$ | = | rate of elastic electron energy exchange |
| $\rho$ | = | density |

*Subscripts*

| | | |
|---|---|---|
| $e$ | = | electron |
| $r$ | = | species |

*Superscripts*

| | | |
|---|---|---|
| $e$ | = | electronic |
| $tr$ | = | translational |

## Introduction

IN the future, space programs will be conducted which will require the efficient return of large payloads from missions to the moon or the planets. To accomplish this task, the return vehicles will utilize either direct entry at very high velocities or aerocapture techniques. In either case, a significant portion of the entry will involve high velocities at high altitudes, and during this part of the trajectory, the vehicle flowfields will be dominated by chemical, thermal, and radiative nonequilibrium phenomena. To design and operate such vehicles, it is essential to understand these chemical, thermal, and radiative nonequilibrium processes and the coupling between them at various flight conditions.

In a companion paper,[1] a viscous shock layer flowfield model for the stagnation region of high-altitude entry vehicles has been developed which includes nonequilibrium chemistry, multitemperature, coupled nongray nonequilibrium radiative transfer for atoms and molecules, and local thermodynamic nonequilibrium (LTNE) phenomena. The objective of this paper is to use this model over a wide range of conditions to investigate the magnitude and extent of nonequilibrium chemical and radiation coupling phenomena in high-altitude entry vehicle flowfields.

## Description of Flowfield Model

The flowfield model used in this investigation is a viscous shock-layer analysis which includes the effects of chemical nonequilibrium, multitemperature thermal nonequilibrium (heavy particle and electron or electron-electronic temperature), and radiative transfer. Radiative gasdynamic coupling is achieved by including in the global energy equation the divergence of the radiative flux, $\nabla \cdot q_r$, and obtaining solutions iteratively. Details concerning the development of this model are in Refs. 1–4.

The radiation analysis is a modified version of RADICAL,[5] which is a detailed method that includes atomic continuum radiation, molecular band radiation, and atomic line radiation for the standard CHON (carbon, hydrogen, oxygen, nitrogen) gas system. To properly model nonequilibrium phenomena, this new radiative model uses actual species concentrations, the appropriate electron-electronic temperature, and modified forms for the source functions and absorption coefficients. These modifications account for the existence of excited state population distributions different from those predicted by a Boltzmann distribution (i.e., local thermodynamic nonequilibrium, LTNE), since non-Boltzmann distributions can significantly affect radiative emission and absorption.

The model also has the option of three different electron-electronic energy models. The first, termed the quasiequilibrium electron model (QEE), is a free electron energy model

Presented as Paper 91-0569 at the AIAA 29th Aerospace Sciences Meeting, Reno, NV, Jan. 7–10, 1991; received Jan. 22, 1991; revision received Aug. 5, 1991; accepted for publication Aug. 27, 1991. 

*NASA Graduate Student Researcher, Aerospace Engineering Department. Student Member AIAA.

†Professor, Aerospace Engineering Department. Associate Fellow AIAA.

in which all derivative terms in the electron energy equation are neglected; and it can be expressed as

$$\dot{w}_e h_e^{tr} - \dot{w}_e \frac{u^2}{2} = \sum_r \xi_{er} + Q_e \tag{1}$$

where the $\xi_{er}$ term account for elastic collisional effects and $Q_e$ represents inelastic effects due to chemical reactions involving electrons. In this model the electronic temperatures are assumed to be equal to the free electron value.

The second is termed the quasiequilibrium electron-electronic energy model (QEEE) and is similar to the first model in that it computes the electron temperature assuming quasi-equilibrium. However, it also accounts for the effects of elastic and inelastic collisions on the energy contained in electronic states of each species as well as the free electron energy, and thus the resulting temperature is representative of electron-electronic energy. The resulting equation is

$$\dot{w}_e h_e^{tr} + \sum_r \dot{w}_r h_r^e - \dot{w}_e \frac{u^2}{2} = \sum_r \xi_{er} + Q_e \tag{2}$$

where the term $\Sigma_r \dot{w}_r h_r^e$ accounts for the production and depletion of electronic energy due to chemical reactions.

The third model utilizes a full combined electron-electronic energy conservation equation which includes the effects of convection, conduction, and diffusion, in addition to the production and loss of electron energy through elastic and inelastic collsions. This full electron-electronic energy equation (FEE) for the stagnation line is

$$\rho u c_p^e \frac{\partial T_e}{\partial n} - \frac{\partial}{\partial n}\left(\eta_e \frac{\partial T_e}{\partial n}\right) - \left(\sum_r \rho \mathcal{D}_r c_{p_r}^e \frac{\partial}{\partial n}\frac{\rho_r}{\rho}\right)\frac{\partial T_e}{\partial n}$$

$$- u \frac{\partial p_e}{\partial n} + \dot{w}_e h_e^{tr} + \sum_r \dot{w}_r h_r^e = \sum_r \xi_{er} + Q_e \tag{3}$$

where

$$c_p^e = c_{p_e}^{tr} \frac{\rho_e}{\rho} + \sum_r c_{p_r}^e \frac{\rho_r}{\rho} \tag{4}$$

For more details concerning the electron-electronic energy models see Refs. 1–2.

Since the present flowfield formulation does not include vibrational nonequilibrium, the above electron-electronic energy models do not include vibrational-electronic coupling. While this phenomena should not be important at higher entry velocities due to the rapid dissociation of diatomic species in and near the shock front, it could be important at lower velocities. Thus, efforts are in progress to include vibrational nonequilibrium and vibrational electronic coupling, and these has been reported in Ref. 6.

## Discussion of Results

Several sets of results obtained using the above methods and models are presented in this section. In all cases, results are for the stagnation streamline, utilize 99 points between the shock front and the wall, and, for simplicity, assume a nitrogen freestream. The nonequilibrium chemistry model is similar to the case II set of Ref. 2 and is shown in Table 1; and it should be representative of high-temperature radiating air. For diffusion, the approximate multicomponent model of Ref. 7 has been used. Since in a high-temperature ionized diatomic gas, charge exchange and ambipolar effects cause atoms, ions, and electrons to all have to a first approximation similar diffusion velocities, such a gas should be dominated by only two diffusion velocities, that of the molecules and that of the atoms, ions, and electrons. For such cases, previous studies[8,9] have shown that the differences between using a constant Lewis number of 1.0 or 1.4 or a variable Lewis number are small, and thus the commonly applied[10] value of 1.4 has been used. Hence, the present model should adequately represent the diffusion phenomena present, including multicomponent effects. In addition, the wall has been assumed to be radiatively black, noncatalytic to atomic recombination, fully catalytic to ionic recombination, and at 1650 K. This value, which corresponds approximately to the maximum possible for a nonablating surface, has been used for convenience and to illuminate cool wall phenomena. However, it is recognized that for many cases of interest the heat transfer load will be more than adequate to induce ablation and to raise the wall temperature to significantly higher values. Finally, in all cases, unless stated otherwise, shock slip is assumed, coupled nongray radiative transfer has been included, and local thermodynamic nonequilibrium effects have been accounted for using the molecular and first order atomic models described in Refs. 1 and 2.

**Table 1 Reaction rate system**

| Reaction | A | B | E |
|---|---|---|---|
| $N_2 + N = 3N$ | $4.085 \times 10^{22}$ | −1.5 | 113100 |
| $N_2 + N_2 = 2N + N_2$ | $4.70 \times 10^{17}$ | −0.5 | 113100 |
| $N_2 + N^+ = N_2^+ + N$ | $2.02 \times 10^{11}$ | 0.8 | 13000 |
| $N + N = N_2^+ + e^-$ | $1.40 \times 10^{13}$ | 0.0 | 67800 |
| $N + e^- = N^+ + 2e^-$ | $4.16 \times 10^{13}$ | 0.5 | 120000 |
| $N + N = N + N^+ + e^-$ | $2.34 \times 10^{11}$ | 0.5 | 120000 |
| $N + N^+ = 2N^+ + e-$ | $2.34 \times 10^{11}$ | 0.5 | 120000 |
| $N_2 + e^- = 2N^+ + e-$ | $3.00 \times 10^{24}$ | −1.6 | 113100 |

Rates in the form $k_f = AT^B \exp(-E/T)$.
$T = T_e$ in electron impact reactions.

### AFE CFD Point 2

This computational fluid dynamics (CFD) condition corresponds to what is often referred to as the "max $Q$" computational point for one of the initial AFE trajectories at which the freestream velocity, pressure, and temperature are 8.915 km/s, 15.715 dynes/cm$^2$, and 197.101K, respectively. For this case the nose radius has been assumed to be 2.3 m, and the electron temperature was required to equal the heavy particle temperature at the wall.

The results, presented on Figs. 1a and 1b, were obtained using the QEE model without the electron impact molecular dissociation reaction, and profiles obtained with both fixed and slip shock jump conditions using a Lewis number of 1.4 are portrayed. As shown, the electron temperature rapidly rises behind the shock front and equilibrates with the heavy particle temperature. However, as evidenced by the continual decrease in temperature and the variations in composition across the shock layer, the stagnation flow for this case is always in chemical nonequilibrium. Also, the wall thermal layer comprises approximately 20% of the 12.2-cm-thick shock layer. For this case, the convective heating was 13.55 W/cm$^2$, the total radiative heat flux to the wall was 1.56 W/cm$^2$, and radiative cooling effects were insignificant.

With respect to temperature, the effects of sip vs fixed shock jump conditions seem to be confined to a small region immediately behind the shock front. However, the impact on concentration and particularly on total enthalpy are significant. In fact, the total enthalpy profiles clearly show that the fixed shock boundary condition results in an incorrect value for enthalpy in the interior of the shock layer, leading to incorrect species concentration values. Interestingly, when a Lewis number of 1 is used with the fixed shock boundary conditions the enthalpy profile appears to be correct and when a value less than unity is used, the enthalpy is high in the flow interior. However, for the shock slip condition, the enthalpy profiles are unaffected by Lewis number. Since a Lewis number of 1.4 is more appropriate for describing atom-molecule diffusion, which is the dominant diffusion mechanism in this flow, and since the enthalpy ratio in the flow interior in the absence of significant radiative cooling should be unity, these

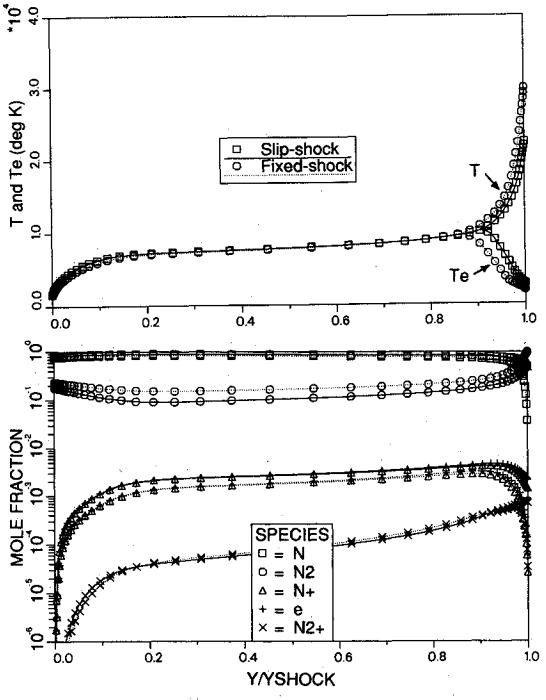


**Fig. 1a Stagnation profiles for AFE CFD point 2 using QEE model, $U$ = 8.915 km/s, $H$ = 77.9 km, $QR$ = 1.56 W/cm², $QC$ = 13.6 W/cm², $YSHOCK$ = 12.2 cm.**

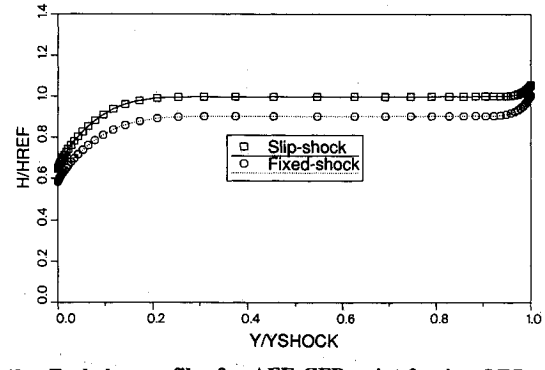


**Fig. 1b Enthalpy profiles for AFE CFD point 2 using QEE model.**

results demonstrate the importance of using slip shock boundary conditions at these conditions. Also, it should be noted that since the results shown on Fig. 1 are for a nitrogen freestream, the radiative heating values in air, based upon comparison with the Fire 2 data,[1] will probably be slightly higher.

### AFE CFD Point 4

This condition corresponds to a "max $Q$" point for a heavier AFE vehicle at which the freestream conditions are 9.326 km/s, 26.4 dynes/cm², and 200 K. Stagnation line temperature and concentration profiles are presented on Fig. 2, which compares results obtained using the QEEE model including the electron impact dissociation reaction with those using the QEE energy model only. The primary effect of using the QEEE model is more extensive thermal nonequilibrium and a lower electron temperature through much of the shock layer. Also, the combined effect of electron impact dissociation and the QEEE model leads to a more dissociated flow having slightly different $N_2$ and $N_2^+$ profiles.

However, the most significant difference in the two models is the radiative heat transfer. For the QEEE case, the lower electron temperature yields a total radiative flux of 1.18 W/cm², a shock standoff distance of 11.96 cm, and a convective heating of 25.8 W/cm². For the QEE model it is 2.91 W/cm², 11.89 cm, and 25.7 W/cm², respectively.

Figure 3a shows the stagnation point continuum and line radiation distributions predicted with the QEEE model. In

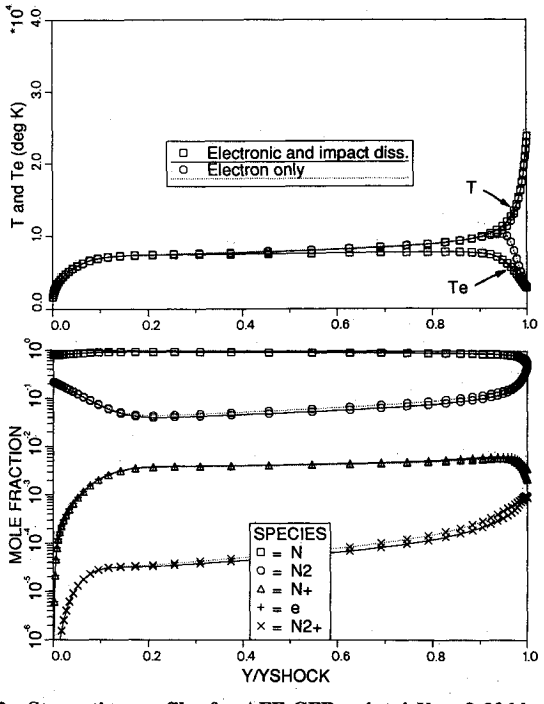


**Fig. 2 Stagnation profiles for AFE CFD point 4 $U$ = 9.326 km/s, $H$ = 75.2 km. For QEEE Case: $QR$ = 1.18 W/cm², $QC$ = 25.8 W/cm², $YSHOCK$ = 12.0 cm. For QEE Case: $QR$ = 2.91 W/cm², $QC$ = 25.7 W/cm², $YSHOCK$ = 11.9 cm.**

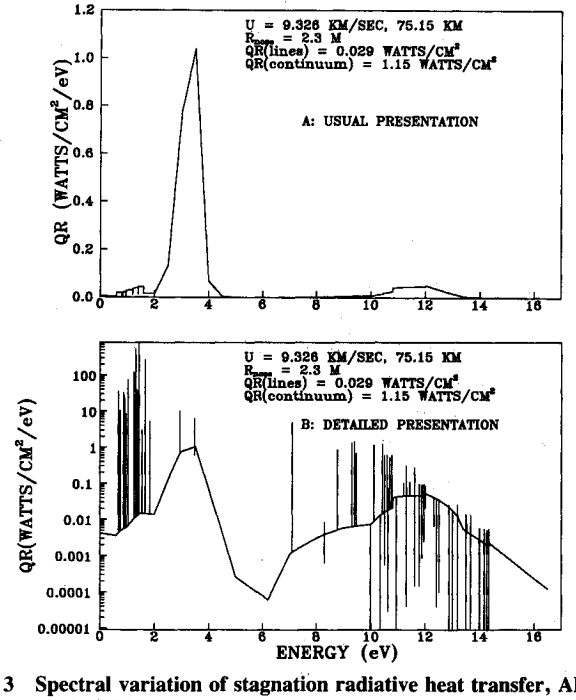


**Fig. 3 Spectral variation of stagnation radiative heat transfer, AFE CFD point 4, QEEE model.**

the actual radiative transfer analysis, lines are considered and integrated individually, but they are presented on Fig. 3a as average values for various line groups for convenience. While there are many infrared line groups and some in the ultraviolet, the line contributions are negligible compared to the continuum. Also, most of the continuum radiation (about 90%) is in the visible and infrared below 6.2 eV; and most of that is between 2 and 4 eV. At these conditions, this radiation is due to the $N_2^+(1-)$ band. In addition, there is some continuum contribution in the ultraviolet, probably due to nitrogen free-bound processes and $N_2$ Birge-Hopfield bands.

Figure 3b shows the same information as Fig. 3a except each line is shown individually. Many of the vacuum ultra-

violet (VUV) lines above 10 eV are absorbing in their line centers, but the infrared (IR) lines are essentially transparent and appear to be strongly emitting. However, line radiation at this condition is insignificant compared to the continuum contribution.

As part of this study computations were also conducted using the QEE model without including molecular LTNE effects; and the resulting radiative heat transfer result was 8.90 W/cm$^2$. Obviously, molecular LTNE is important at AFE conditions and leads to lower radiative heating. Examination of the results indicate that the LTNE induced by chemical and thermal nonequilibrium drastically reduces radiation from the $N_2(1+)$ and $N_2(2+)$ bands and significantly decreases that due to $N_2$ Birge-Hopfield. However, $N_2^+(1-)$ is virtually unaffected by chemical and thermal nonequilibrium phenomena. Thus, on Fig. 3, the primary stagnation point radiation is in the continuum between 2 and 4 eV and is from the $N_2^+(1-)$ band.

At shock speeds below 10 km/s, shock tube radiative intensity photomultiplier measurements indicate a sharp rise to a peak immediately behind the shock front followed by a decrease until equilibrium is achieved.[11] Similar results have been obtained computationally for nonequilibrium flows for the visible region of the spectrum assuming the gas to be transparent.[12] Figure 4 shows for the present QEEE model the variation along the stagnation line of radiative flux towards the stagnation point, $QR+$, and its negative derivative, $-D(QR+)/DY$. The latter is essentially what Candler[12] and others have termed radiation intensity. As can be seen, $-D(QR+)/DY$ is similar to observed photomultiplier traces in having a peak near the shock front followed by a steady decrease towards the wall. For this case, no equilibrium plateau is achieved since the flow never reaches chemical equilibrium prior to the wall thermal boundary layer. (The oscillations near the wall are an artifact due to significant digit error resulting from providing the plot routine formatted data. The actual curve is smooth.) Comparison with the temperature plots indicates that the "intensity" peak corresponds to the maximum value in electron temperature, and near the wall the "intensity" is negative, indicating absorption. However, as shown by only the slight decrease in $QR+$, the amount of absorption near the wall is negligible at these conditions.

### High-Speed Mars Return Case

In a recent paper,[13] results have been presented for the stagnation line of a one meter nose radius body at a trajectory point of 14.5 km/s at 65 km, which is representative of a high-speed Earth entry return from Mars. These results include chemical nonequilibrium, thermal nonequilibrium assuming that the vibrational, electronic, and electron temperatures can be represented by a single temperature and uncoupled nonequilibrium radiation. The investigators obtained for this trajectory point an uncoupled radiative heating rate of 1700 W/cm$^2$, a shock standoff distance of 5.7 cm, and a postshock chemical nonequilibrium zone 1.1 cm thick in which the electron-electronic vibrational temperature never significantly exceeded the equilibrium temperature. They also stated that most of the radiative heating was from the ultraviolet below 2000 A, that it originated from the nonequilibrium region behind the shock wave, and that very little was absorbed in the wall thermal layer. The latter is different from previous beliefs by some researchers[14] but is in agreement with approximate studies.[3] In addition, separate results were obtained for the same case with an equilibrium viscous shock-layer method[15] that used a coupled radiation model similar to RADICAL, and these predicted a standoff distance of 3.5 cm and a radiative heating rate of 970 W/cm$^2$.

To investigate these differences, the present model using the full electron-electronic energy model with LTNE effects and a partially catalytic wall has been applied to this case; and temperature and ionization profiles are presented on Fig. 5. Here, the predicted shock standoff distances are 3.92 cm and 3.67 cm for the radiatively uncoupled and coupled cases respectively, and most of the shock layer is in chemical equilibrium. The difference in the standoff lengths between the present results and the nonequilibrium result of Ref. 13 is believed to be primarily due to the electron temperature profile and its subsequent effect on chemistry. In Ref. 13 $T_e$ is low in the region behind the shock front, possibly due to the combining of electron-electronic with vibrational phenomena. However, the present results show significant dissociation at the shock front with diatomic species being insignificant over most of the shock layer and ionization dominating the chemistry. Thus, in the present case the FEE energy model is strongly influenced by collisional and ionization phenomena, and $T_e$ significantly exceeds the equilibrium temperature in the nonequilibrium zone. Since the dominant ionization mechanism behind the shock front is electron impact[2] which is governed by free electron temperature, this enhancement of $T_e$ accelerates ionization, shortens the chemical nonequilibrium zone to about 0.3 cm, and decreases the overall shock-layer thickness. However, as expected, the present thickness prediction is greater than that for the equilibrium case discussed above. It should also be noted that the difference

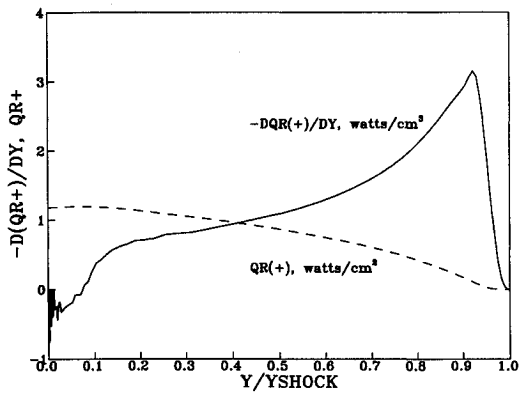


**Fig. 4 Intensity and radiative flux towards stagnation point, AFE CFD point 4, QEEE model.**

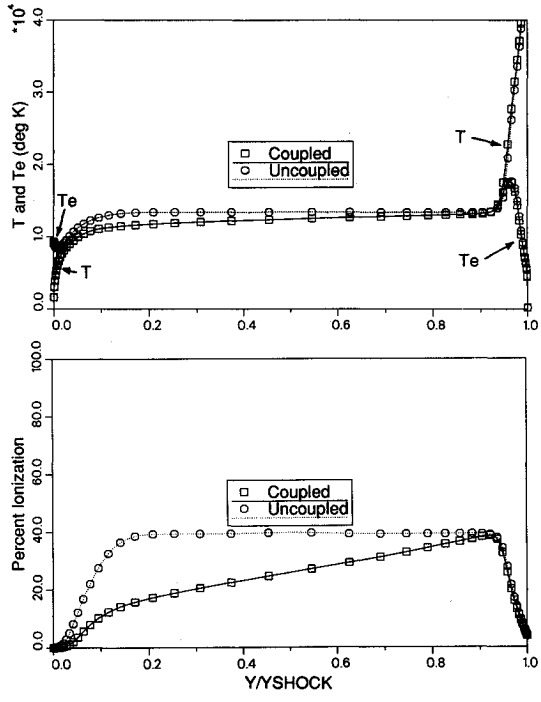


**Fig. 5 Stagnation profiles at 14.5 km/s, 65 km, Rnose = 1 m. Uncoupled: $QR$ = 2831 W/cm$^2$, $QC$ = 426 W/cm$^2$, $YSHOCK$ = 3.92 cm. Coupled: $QR$ = 1347 W/cm$^2$, $QC$ = 430 W/cm$^2$, $YSHOCK$ = 3.67 cm.**

between the present results and those of Ref. 13 show the strong sensitivity of solutions to electron temperature models at such trajectory points.

Results obtained with the present model predict the stagnation point radiative heat transfer for the case without any radiation gasdynamic coupling to be 2831 W/cm$^2$, which is higher than that of Ref. 13. Comparison of the spectral variation of the stagnation point radiative flux indicates that the present results have significant radiation above 11 eV, primarily due to free-bound continuum processes, while those of Ref. 13 have little or no flux in this region. Since both methods treat lines in detail, and since both have previously been shown to be in reasonable agreement in the visible and infrared, it appears that the differences are primarily due to the treatment of atomic continuum radiation in the vacuum ultraviolet. It should be noted that the present radiation model has for equilibrium conditions shown good agreement with experimental data over the total spectrum.[16] Further, the present results indicate that most of the radiation originates from the high-temperature equilibrium portion of the shock layer in the range $0.4 < y/YSHOCK < 0.9$ and not from the postshock nonequilibrium zone. In the latter, chemical nonequilibrium induces extensive local thermodynamic nonequilibrium and depopulates the excited states rapidly via ionization with the result that very little radiation originates in the nonequilibrium region.

Moreover, the radiation coupled results for this case indicate significant radiation cooling, as evidenced by the decrease in radiative heating to 1347 W/cm$^2$ and by the steady decrease in temperature and ionization throughout the equilibrium zone. Further, while the equilibrium coupled prediction for this case was only 970 W/cm$^2$, it is probable that the difference between it and the present prediction is due to the influence of reaction chemistry, differences in assumed wall catalycity, and the amount of absorption in the wall thermal layer. Basically, equilibrium chemistry should predict more molecules and, hence, more absorption. This possibility is supported by the equilibrium results which indicate that the wall thermal layer absorbs about 32% of the wall directed flux while in the present model only about 20% is absorbed. Thus, while most of the shock layer is in chemical equilibrium, nonequilibrium effects may still be important and affect the radiative heatings, and, obviously, radiation cooling is important for this case and needs to be included in an analysis model.

#### Velocity Effects at 80 km

Results have been obtained using the FEE model for a 2.3-m nose radius vehicle for three different velocities, 12, 14, and 16 km/s, at an altitude of 80 km. These velocities are, depending upon the trajectory chosen, within the possible range of entry speeds associated with certain Martian and Lunar return vehicles.

The temperature and composition profiles for the 12 km/s case are shown on Fig. 6; and, as shown by the continually decreasing temperature and the variation in the $N^+$ concentration, the entire shock layer at this flight condition is in chemical nonequilibrium. Immediately behind the shock front, which is 11.5 cm from the wall, the electron-electronic temperature slowly rises to a peak value and then gradually equilibrates with the heavy particle temperature. In the wall thermal layer, which comprises about 20% of the shock layer, deionization and recombination processes are important. For this case, when radiative coupling and LTNE effects are included, the radiative heat transfer is 24.3 W/cm$^2$ and the convective rate is 33 W/cm$^2$.

The temperature and composition profiles for the 14 km/s case are shown on Fig. 7. Since the freestream velocity is higher, the postshock nonequilibrium zone is shorter than at 12 km/s, occupying only the outer 30–40% of the 9.1-cm shock layer. The electron-electronic temperature rises rapidly and peaks at a value several thousand degrees above the equilibrium temperature, and the wall sheath representation only affects the electron temperature in a small zone near the wall. For this case the convective heating is 56.4 W/cm$^2$ and the radiative flux is 110.7 W/cm$^2$. Interestingly, especially when compared to the AFE cases, only about 10% of this radiative heating is due to molecular processes.

As part of this study, several cases were also conducted at this condition using the QEEE and QEE energy models; and the only difference between the models was that the peak in electron temperature was slightly higher and slightly farther from the shock front with the exact model than with the quasiequilibrium models. This behavior has been observed at freestream velocities of 12 km/s and higher and is in sharp

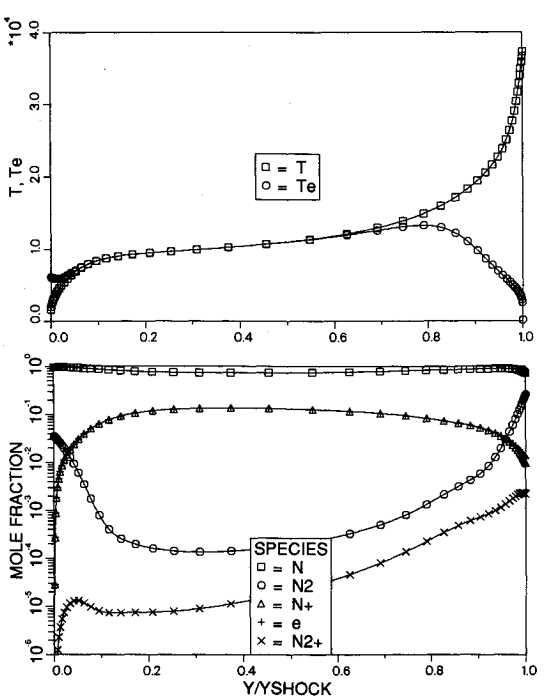


Fig. 6 Coupled stagnation profiles at 12 km/s, 80 km, Rnose = 2.3 m. *QR* = 24.3 W/cm$^2$, *QC* = 33 W/cm$^2$, *YSHOCK* = 11.5 cm.

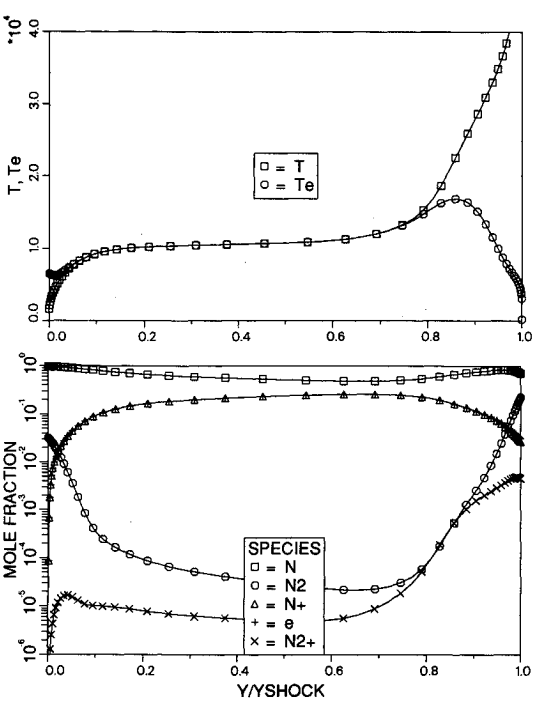


Fig. 7 Coupled stagnation profiles at 14 km/s, 80 km, Rnose = 2.3 m. *QR* = 111 W/cm$^2$, *QC* = 56.4 W/cm$^2$, *YSHOCK* = 9.1 cm.

contrast to the trends displayed at the AFE velocities. At the higher velocities there are more electrons, and the flow is dominated by ionization processes. Consequently, the electron-electronic energy is dominated by the free electrons. At the lower AFE speeds, there is very little ionization and the electronic energy portion dominates the combination. Thus, the shape and character of the electron temperature profiles appears to be significantly different at the higher velocities than at AFE speeds.

The spectral variation in radiative heat flux to the wall at 14 km/s is shown on Fig. 8a, where the contributions due to line and continuum processes have been combined and the convenient representation of lines as group averages has been utilized. Here, the heating due to continuum and lines is similar in magnitude with extensive infrared and ultraviolet (UV) lines as well as significant VUV bound-free processes. In fact, only about 28% of the wall flux is from the visible and infrared below 6.2 eV. Notice that a measurable portion of the visible radiation is between 2 and 4 eV and is due to $N_2^+(1-)$ molecular radiation.

As mentioned previously, the actual radiative transfer analysis treats lines individually, and Fig. 8b displays the same information as Fig. 8a but with each line shown separately. From this representation, it is evident that in the visible and infrared the line radiation is primarily transparent. However, in the VUV, many of the line centers are highly absorbing, and careful examination of the spectral distribution shows that most of the line emission reaching the wall originates from the line wings.

In contrast to results below 10 km/s, shock tube photomultiplier results at higher speeds show that the radiative intensity peak behind a shock front changes from a single peak to a double hump peak system.[11] Experimental spectral data indicates that the first is due to molecular radiation near the shock front, while the second is atomic radiation coupled to the ionization process. Figure 9 shows for the 14 km/s condition theoretical predictions of the radiative flux towards the wall, $QR+$, and the negative of its derivative, $-DQR(+),DY$. As discussed previously, the latter is closely related to radiative intensity.

The present profile clearly exhibits this double hump behavior. The first peak corresponds to the maximum value of the electron temperature, while the second occurs at the onset of thermal equilibrium and the establishment of near Boltzmann distributions in the excited states. Subsequently, radiative cooling occurs and the "intensity" rapidly decreases. During this period, examination of the species concentrations and of LTNE phenomena indicates nonequilibrium recombination is induced with resultant overpopulation, compared to a Boltzmann distribution, of the excited states. Around *y/YSHOCK* of 0.3 the flow begins to absorb more than it emits and $QR+$ begins to decrease. However, as shown by the $QR+$ profile, which only decreases slightly between 0.3 and the wall, the absorption in the wall thermal layer only results in a mild decrease in $QR+$ at this condition.

The temperature and composition profiles at 16 km/s are shown on Fig. 10, and the corresponding predicted radiative and convective heating rates are 272.6 and 87.3 W/cm², respectively. Here, the electron temperature rises very rapidly and peaks near 20,000 K, confirming the trend that as speed increases, the peak electron-electronic temperature increases in magnitude and occurs nearer to the shock front. Likewise, again due to the increase in velocity, the nonequilibrium zone is shorter at about 20–25% of the 7.5-cm shock layer. Finally, on Fig. 10 notice that radiation cooling effects induce both atomic and ionic recombination starting near the end of the postshock nonequilibrium zone and continuing all the way to the wall.

The effect on the temperature and ionization profiles of

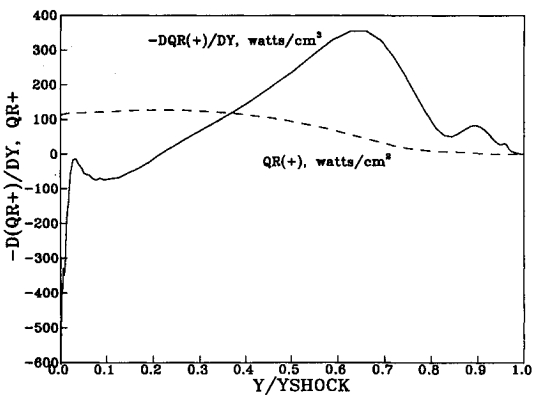


**Fig. 9 Intensity and radiative flux towards stagnation point, 14 km/s, 80 km.**

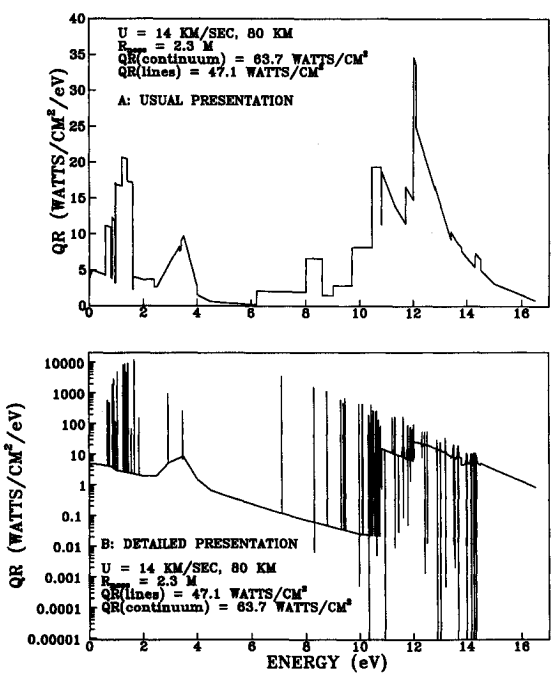


**Fig. 8 Spectral variation of stagnation radiative heat transfer, 14 km/s, 80 km.**

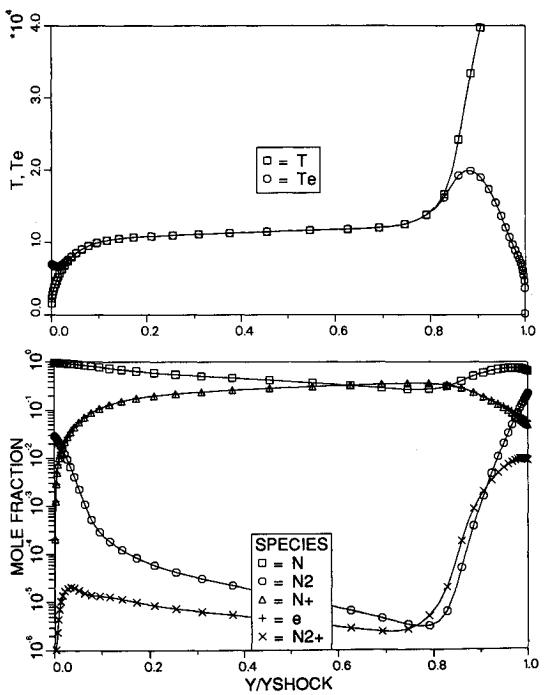


**Fig. 10 Coupled stagnation profiles at 16 km/s, 80 km, Rnose = 2.3. *QR* = 273 W/cm², *QC* = 87.3 W/cm², *YSHOCK* = 7.5 cm.**

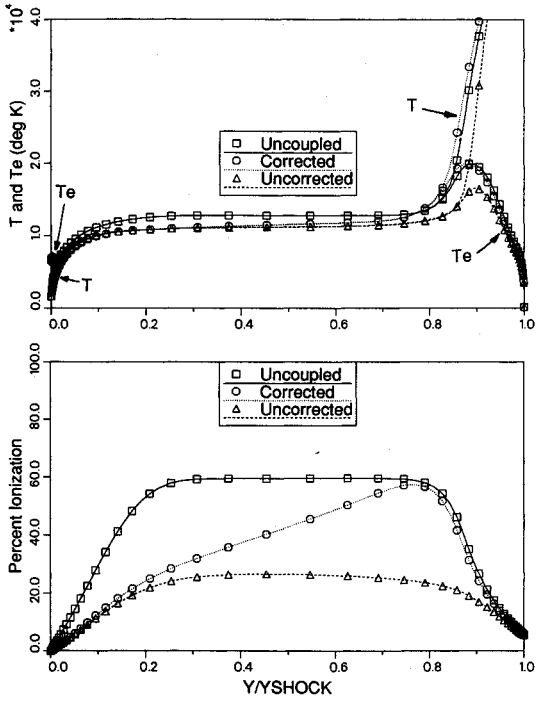


Fig. 11 LTNE and coupling effects at 16 km/s and 80 km.

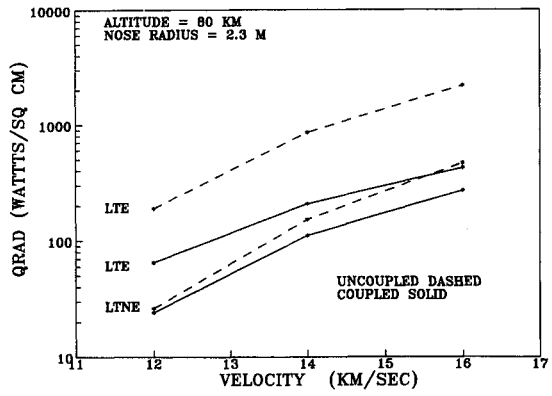


Fig. 12 LTNE and coupling effects on radiative heat transfer.

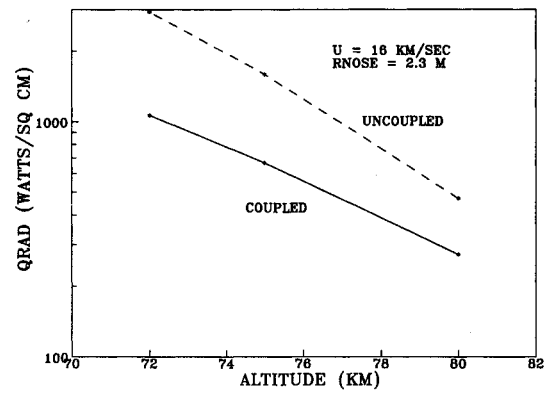


Fig. 13 Radiative gasdynamic coupling effects on radiative heat transfer.

including radiative gasdynamic coupling in the flowfield and local thermodynamic nonequilibrium effects in the radiation is shown for the 16 km/s case on Fig. 11. The curves denoted "Uncoupled" do not include either radiation cooling or LTNE phenomena and indicate for this case that nominally the nonequilibrium post-shock zone and the wall thermal layer each affect about 20% of the shock layer. For this case, the shock standoff distance is 8.16 cm. However, when radiation coupling is included but LTNE is excluded, the shock-layer thickness is reduced to 7.15 cm due to the lower temperature and increased density. The resultant profiles, designated as "Uncorrected," show that without LTNE effects significant cooling occurs in the nonequilibrium region with corresponding decreases in the electron and heavy particle temperatures and in the apparent length of the relaxation zone. Further, radiative losses through the shock front from the high-temperature nonequilibrium zone reduce the total enthalpy 40%, which leads to a cooler equilibrium zone having less than half the ionization of the uncoupled case.

Fortunately, when both radiation coupling and LTNE effects are included, the radiative losses are much less. As shown on the curves denoted as "Corrected," the corresponding temperature and ionization variations in the nonequilibrium post-shock region are only slightly affected since in that region the radiative losses are low due to LTNE effects. However, once equilibrium is nearly established around 0.8, radiative cooling becomes the dominant feature, the temperature steadily decreases, and the degree of ionization rapidly decreases. Obviously, at these conditions both LTNE phenomena and radiation coupling are important and need to be included.

A graphical summary of the 80-km radiative heating results is presented as Fig. 12, and several interesting features are evident. First, the inclusion of LTNE significantly affects the predicted radiative heat transfer at all three flight velocities, independent of whether or not radiative coupling is included. Second, the amount of radiative cooling is lower in the LTNE corrected predictions as compared to the local thermodynamic equilibrium (LTE) uncorrected flows; and, third, when both phenomena are properly included, radiative cooling ranges from relatively minor at 12 km/s to significant at 16 km/s.

Finally, for all three flight velocities, the predicted radiative heating is significant compared to the convective heating, and in the 16 km/s case the radiative heating is about three times the convective value. Since it is anticipated that advanced heat shield materials can withstand 70 W/cm$^2$ without ablating, these results indicate that at 80 km nonablative heat shields possibly could be used up to about 12.5 km/s.

### Altitude Effects at 16 km/s

In order to investigate altitude effects and to use the model under a situation on a vehicle where most of the shock layer is in equilibrium, results have been obtained for the 2.3-m body at 16 km/s at 75 and 72 km as well as at 80 km. Since the resultant profiles do not exhibit any new phenomena, they are not shown. However, as the pressure increases with decreasing altitude, the postshock nonequilibrium chemical relaxation zone decreases significantly so that by 72 km it only encompasses about 5% of the shock layer. At that condition, the present model predicts a shock layer thickness of 7.05 cm, and radiative and convective heating rates of 1064 and 209 W/cm$^2$. Also, since the extent of nonequilibrium decreases with altitude, LTNE phenomena decrease and have a minor effect on the coupled radiative heat transfer predictions by 72 km. However, as shown on Fig. 13, radiative coupling/cooling is important at all three altitudes and increases as altitude decreases. Interestingly, the coupled results at 72 and 75 km, which have nearly equilibrium shock layers, are in excellent agreement with the equilibrium radiative heating predictions of Ref. 17. However, the present nonequilibrium radiative predictions at 80 km are higher than the equilibrium values of Ref. 17 at both 14 and 16 km/s.

## Conclusions

In this paper a viscous shock layer engineering flowfield model suitable for analyzing the stagnation region of high-altitude entry vehicles having extensive chemical and radiative nonequilibrium has been applied to a variety of cases including two AFE trajectory points, a condition representative of the high-speed return from Mars of a small vehicle, a series of points at 80 km for velocities 12 to 16 km/s, and a study of

the effects of altitude at 16 km/s. Based on these results the following conclusions can be stated:

1) Shock slip phenomena are important at all conditions investigated.

2) Radiation cooling/coupling is important for many cases. Specifically, a) it is a minor effect for the AFE conditions investigated; b) at 80 km, it is small at 12 km/s, important by 14 km/s, and very significant at 16 km/s at all altitudes; and c) it is very important for the high-speed Mars return case.

3) Radiation heat transfer should be included and varies as to spectral origin. Specifically, a) for the AFE, radiation, while small, is important and primarily molecular, $[N_2^+(1-)]$. b) At 12 km/s and above radiation is a significant portion of the total heating and is primarily due to atomic processes. By 14 km/s it is the dominant heating mechanism.

4) Local thermodynamic nonequilibrium is important and should be included in all models. In addition, a) LTNE depopulates the excited states of atoms and $N_2$ molecules in the postshock nonequilibrium region. b) LTNE can lead to an overpopulation of excited states in regions of radiative cooling and in the wall thermal layer. c) $N_2^+(1-)$ is relatively unaffected by LTNE. d) The importance of LTNE is independent of radiative coupling. e) The inclusion of LTNE reduces the magnitude of radiation cooling effects.

## Acknowledgments

This work was primarily supported by NASA Grant NAG-1-1003 from the Langley Research Center, with Lin C. Hartung as technical monitor. T. A. Gally is partially supported by a NASA Graduate Student Researchers Fellowship through the NASA Johnson Space Center.

## References

[1]Gally, T. A., and Carlson, L. A., "Nonequilibrium Chemical and Radiation Coupling, Part I: Theory and Models," *Journal of Thermophysics and Heat Transfer*, Vol. 6, No. 3, 1992, pp. 385–391.

[2]Carlson, L. A., and Gally, T. A., "The Effect of Electron Temperature and Impact Ionization on Martian Return AOTV Flowfields," *Journal of Thermophysics and Heat Transfer*, Vol. 5, No. 1, 1991, pp. 9–20.

[3]Carlson, L. A., "Approximations for Hypervelocity Nonequilibrium Radiating, Reacting, and Conducting Stagnation Regions," *Journal of Thermophysics and Heat Transfer*, Vol. 3, No. 4, 1989, pp. 380–388.

[4]Carlson, L. A., Bobskill, G. J., and Greendyke, R. B., "Comparison of Vibration Dissociation and Radiative Transfer Models for AOTV/AFE Flowfields," *Journal of Thermophysics and Heat Transfer*, Vol. 4, No. 1, 1990, pp. 16–26.

[5]Nicolet, W. E., "User's Manual for the Generalized Radiation Transfer Code (RAD/EQUIL or RADICAL)," NASA CR 116353, Oct. 1969.

[6]Gally, T. A., Carlson, L. A., and Green, D., "A Flowfield Coupled Excitation and Radiation Model for Nonequilibrium Flows," AIAA Paper 91-1463, June 1991.

[7]Miner, E. W., and Lewis, C. H., "Hypersonic Ionizing Air Viscous Shock Layer Flows over Nonanalytic Blunt Bodies," NASA CR-2550, May 1975.

[8]Carlson, L. A., and Nerem, R. M., "Equilibrium Air Stagnation Point Boundary-Layer Calculations Using a Variable Heat of Dissociation Model," *Journal of Heat and Mass Transfer*, Vol. 11, 1968, pp. 699–707.

[9]Moss, J. N., "Reacting Viscous Shock Layer Solutions with Multicomponent Diffusion and Mass Injection," NASA Technical Report TR-R-411, June 1974.

[10]Rose, P. H., and Stark, W. I., "Stagnation Point Heat-Transfer Measurements in Dissociated Air," *Journal of Aerospace Sciences*, Vol. 25, Feb. 1958, pp. 86–97.

[11]Wilson, J., "Ionization Rate of Air Behind High Speed Shock Waves," *The Physics of Fluids*, Vol. 9, No. 10, 1966, pp. 1913–1921.

[12]Candler, G., and Park, C., "The Computation of Radiation from Nonequilibrium Hypersonic Flows," AIAA 88-2678, June 1988.

[13]Park, C., and Milos, F. S., "Computational Equations for Radiating and Ablating Shock Layers," AIAA Paper 90-0356, Jan. 1990.

[14]Park, C., "Assessment of Two Temperature Kinetic Model for Ionizing Air," *Journal of Thermophysics and Heat Transfer*, Vol. 3, No. 3, 1989, pp. 233–244.

[15]Nicolet, W. E., Waterland, L. R., and Kendall, R. M., "Methods for Predicting Radiation Coupled Flowfields about Planetary Entry Probes," *Aerodynamic Heating and Thermal Protections Systems*, edited by L. S. Fletcher, Vol. 59, Progress in Astronautics and Aeronautics, AIAA, New York, 1978, pp. 120–136.

[16]Sutton, K., "Air Radiation Revisited," *Thermal Design of Aeroassisted Orbital Transfer Vehicles*, edited by H. F. Nelson, Vol. 96, Progress in Astronautics and Aeronautics, AIAA, New York, 1985, pp. 419–442.

[17]Sutton, K., and Hartung, L. C., "Equilibrium Radiative Heating Tables for Earth Entry," NASA TM 102652, May 1990.